

Physical characterization and modeling of candidate Hyper-Compact HII Regions

I. T. Rodríguez-Esnard^{*1,2}, S. Kurtz³, J. D. Pandian⁴, J. Franco⁵,
A. Sánchez-Monge^{6,7}, M. A. Trinidad¹, V. Migenes⁸

¹Departamento de Astronomía, Universidad de Guanajuato, Guanajuato, México.

²Instituto de Cibernética, Matemática y Física, Cuba

³Instituto de Radioastronomía y Astrofísica, Universidad Nacional Autónoma de México, México.

⁴Department of Earth & Space Science, Institute of Space Science & Technology, India.

⁵Instituto de Astronomía, Universidad Nacional Autónoma de México, México.

⁶Institute of Space Sciences (ICE-CSIC), Barcelona, Spain

⁷Institute of Space Studies of Catalonia (IEEC), Barcelona, Spain

⁸Department of Physics, Texas Southern University, Texas, USA

Abstract

Hypercompact HII regions (HC) are regions of ionized gas associated with the early stages of high-mass star formation. With the aim of better understanding their characteristics, we studied five candidate HC HII regions. Here, we present observations with the Jansky Very Large Array (VLA) at 2 and 6 cm, with angular resolutions in the range of $\sim 1 - 3''$ and report the images of the detected sources and the measured parameters. In addition, we explore several possible scenarios, considering the regions as both uniform and non-uniform spheres, and as winds, both spherical and collimated. In most cases, the sources were unresolved, but by applying the models, we estimate that their sizes vary in a range of 0.3 to 3.7 mpc while their electron densities are in the range of 1.3×10^5 to $2.4 \times 10^6 \text{ cm}^{-3}$, indicating that most sources are consistent with small, weak UC HII regions, although a few remain viable candidates for HC HII regions, with G40.28–0.22 as the strongest case. We do not rule out the possibility that some sources are jets or stellar winds.

Keywords: HII regions, Stars: formation, Stars: massive

Resumen

Las regiones HII hipercompactas son regiones de gas ionizado asociadas con las etapas tempranas de formación de estrellas de alta masa. Realizamos un estudio de cinco candidatas a regiones HII HC, con el objetivo de comprender mejor sus características. Para esto se llevaron a cabo observaciones con el Jansky Very Large Array (VLA) en 2 y 6 cm, con resoluciones angulares en el rango de $\sim 1 - 3''$ y reportamos las imágenes de las fuentes detectadas y los parámetros medidos. Además, exploramos varios escenarios posibles, considerando las regiones como esferas (uniformes y no-uniformes) y como vientos (esféricos tanto como colimados). En general, las fuentes fueron no-resueltas, sin embargo, al aplicar los modelos, hemos podido estimar que sus tamaños varían en un rango de 0.3 a 3.7 mpc y que las densidades electrónicas están en el rango de 1.3×10^5 a $2.4 \times 10^6 \text{ cm}^{-3}$, lo que indica que la mayoría de las fuentes son consistentes con pequeñas y débiles regiones UC HII, aunque algunas siguen siendo candidatas viables a regiones HC HII, destacando G40.28–0.22 como el caso más fuerte. No descartamos la posibilidad de que algunas fuentes sean chorros o vientos estelares.

*Corresponding author: it.rodriguez@ugto.mx

1 Introduction

Hypercompact (HC) HII regions are a class of ionized gaseous nebulae, linked to the early phases of high-mass star formation. They are commonly located within dusty clumps, associated with masers, outflows, broad radio recombination lines, and extended green objects [Yang et al., 2021]. These regions have distinctive properties that set them apart from other HII regions, such as compact and ultracompact HII regions: they are smaller ($\lesssim 0.05$ pc), with higher electron densities ($n_e \gtrsim 10^6$ cm $^{-3}$) and extremely high emission measures ($EM \gtrsim 10^9$ pc cm $^{-6}$) [Kurtz, 2002].

It is expected that HC HII regions are optically thick at centimeter wavelengths. This characteristic leads to a positive spectral index (α , Kurtz [2005]) indicating that the observed brightness increases with frequency. There are different theories to account for the properties of HC HII regions with an intermediate spectral index ($\alpha \sim +1$) in the optically thick regime rather than the canonical value of +2 for an optically thick, uniform density region. It has been proposed that they are composed of multiple unresolved clumps of gas [Ignace and Churchwell, 2004] or that they have density gradients [Franco et al., 2000].

The small sizes of HC HII regions can be explained by models of photo-evaporating disk winds [Hollenbach et al., 1994, Lizano et al., 1996, Lugo et al., 2004]. Alternatively, HC HII regions can be explained by ionized accretion flows, where the stellar mass gradually increases due to accretion through the HC HII region [Keto, 2003]. Tan and McKee [2003] proposed that high accretion rates for massive young stellar objects lead to higher outflow rates, creating small, jet-like HC HII regions confined by their outflows. The extremely broad radio recombination lines observed in some HC HII regions can be attributed to bulk gas motions such as accretion, rotation, or expansion, with some contribution from pressure broadening [Lizano, 2008].

Unfortunately, there is no large sample of known hypercompact (HC) HII regions to study their properties in a statistically significant way. Some progress in this regard has recently been made by two groups. Yang et al. [2021] identified 16 HC HII regions in a sample of 120 HII regions, while Patel et al. [2023, 2024, 2025] report 46 confirmed and/or candidate HC HII regions. Our previous studies discovered six candidate HC HII regions within a sample of 24 HII regions using an angular resolution of 6'' and 9'' [Sánchez-Monge et al., 2011]. However, they were not able to spatially resolve the sources and place strong constraints on their properties. They inferred that these regions are very compact, with sizes between 1 and 10 mpc and spectral indices between 0.4 and 1.4. In this paper, we investigate five HC HII region candidates from Sánchez-Monge et al. [2011] by conducting new observations at 2 and 6 cm to better constrain the source properties.

We outline the observations and the data reduction methods in section §2. Section §3 reports our observational results. Section §4 applies various models to estimate the physical parameters of the sources, and section §5 discusses our findings for each source. In section §6 we discuss our main results and summarize the main conclusions of our study.

2 Observations

We observed five candidate HC HII regions, which were selected from Sánchez-Monge et al. [2011] because they show 6.7 GHz methanol maser emission (a tracer of high-mass star formation) and they show little or no emission at 6 or 20 cm (suggesting a pre-ultracompact HII region stage). All sources show extended 8 and 24 μ m emission, further supporting their identification as very young high-mass star-forming regions. The sources are listed in Table 1.

The observations were made with the Jansky Very Large Array (VLA) of the NRAO¹ in the 6

¹The National Radio Astronomy Observatory (NRAO) is a facility of the National Science Foundation operated

and 2 cm (5.8 and 14.5 GHz) continuum emission using the B and C configurations, respectively, during two observing runs in February and June 2012 (project code VLA/12A-145). The observations were made in scaled-arrays, so the synthesized beams were expected to be approximately the same ($\sim 0.9''$) at both wavelengths. However, during the 2 cm C-array observation, about one-third of the antennas did not have 2 cm receivers installed, resulting in a larger beam of $\sim 2''$.

The observations at both wavelengths were made with a bandwidth of 2048 MHz comprised of 16 spectral windows, each containing 128 1-MHz channels at 6 cm and 64 2-MHz channels at 2 cm. Right and left circular polarizations were sampled, and the on-source integration time for each field was 10 minutes.

The amplitude and bandpass calibrator used was J1331+305 (3C286) with a calculated flux density of 6.4 Jy at 6 cm and 3.6 Jy at 2 cm using the Perley and Butler 2010 scale. The phase calibrators were J1851+0035 (for G34.82+0.35 and G40.28-0.22) with flux densities of ~ 0.8 Jy and ~ 1.0 Jy at 6 cm and 2 cm, respectively and J1922+1530 (for G48.99-0.30, G53.04+0.11, and G53.14+0.07) with flux densities of ~ 0.4 Jy and ~ 0.3 Jy at 6 cm and 2 cm, respectively.

In addition, we used previous observations from [Sánchez-Monge et al. \[2011\]](#). To ensure a uniform treatment of all the data, we reduced their observations at 3.6 and 1.3 cm using the same procedures as for the new data at 2 and 6 cm. Calibration and imaging were performed using the software CASA. The observing parameters of the maps (beam size and rms noise), as well as some properties of the regions (kinematic distances and luminosities), are given in Table 1.

3 Observational Results

The five regions observed were previously reported by [Sánchez-Monge et al. \[2011\]](#) using lower angular resolutions of approximately $9''$ and $6''$ at 3.6 and 1.3 cm, respectively, which are roughly six times lower than our resolution of $0.9''$. With our higher resolution observations, we were able to resolve several sources into multiple components.

We detected continuum emission at 2 and 6 cm toward all regions and confirmed the previous detections at 3.6 and 1.3 cm, (see Figure 1). We find that two of the candidates for HC HII reported by [Sánchez-Monge et al. \[2011\]](#) are multiple systems (G53.04+0.11 and G53.14+0.07), and we made a new detection of one source (G53.04+0.11nw). The remaining three HC HII regions are single-component sources (G34.82+0.35, G40.28-0.22 and G48.99-0.30). We detected a total of 10 sources in the five observed regions, which are very compact ($\lesssim 20$ mpc) and mostly appear as unresolved sources. In addition, their flux densities are mostly between 0.1 and 1 mJy, except for G48.99-0.20, which is about ~ 10 times stronger.

In Table 2 we report the peak positions (from the highest angular resolution 6 cm images), the integrated flux densities (at all four wavelengths), and the measured source sizes (at 6 cm) defined as half the geometric mean of the major and minor axes, which were determined by fitting 2-D Gaussians with CASA. We used 6 cm images for these fits because they have better resolution and uv -coverage than the 2 cm images. The flux densities were measured with the IMFIT task in CASA, which fits two-dimensional Gaussians to the image data. Most of the sources were unresolved, so the integrated flux obtained is equivalent to that of a point source. In the few cases with indications of resolved emission, IMFIT consistently recovered the total flux. We also report in Table 2 the observed brightness temperature and the spectral index obtained from a linear least squares fit to $S_\nu \propto \nu^\alpha$ between 1.3 and 6 cm. In most cases the spectral index is consistent with thermal free-free emission from (partially optically thick) HII regions or, alternatively, collimated/spherical winds. We discuss both scenarios below.

under cooperative agreement by Associated Universities, Inc.

4 Models and Methods applied

4.1 HII regions

The evolution of HII regions is a complex process that develops in clouds of varying densities. These regions may start in cores of constant density and spread toward areas where the density decreases following a power law. During the formation and expansion of HII regions, there is a critical exponent that plays a crucial role, as it determines whether the cloud will be completely ionized or not [Franco et al., 1990]. If the power-law exponent exceeds 1.5, the HII region may enter the so-called champagne phase, characterized by supersonic expansion. Furthermore, in disk-shaped clouds, this evolution can lead to the appearance of neutral, high-velocity outflows.[Franco et al., 1989].

To interpret the radio spectra of small HII regions, we use models from Olzon [1975] to estimate the physical parameters for spherical, cylindrical, and Gaussian geometries, using the equations in appendix A. We fit the flux density as a function of frequency by adjusting the free parameters of the equations which are the radius, R , and the electron density, n_e , for an isothermal 10^4 K plasma.

We found that the results from the three models were very similar for each source, with the parameters R and n_e predicted by the models falling within the errors of the fit (Figure 3). For simplicity, we present the results for the spherical distribution case only. In addition, we report the emission measure, optical depth, ionized mass, and minimum Lyman continuum photon flux obtained from the spherical models. The ionized mass was calculated assuming a homogeneous sphere of ionized hydrogen of radius R and electron density n_e , using $M_i = \frac{4}{3}\pi R^3 n_e m_p$. The minimum Lyman continuum photon flux was derived by equating ionizations and recombinations in the same volume, with $N_{Ly} = \frac{4}{3}\pi R^3 n_e^2 \alpha_B$, where α_B is the case B recombination coefficient for 10^4 K gas. Varying the electron temperature between 8,000 and 11,000 K produces about a 10% change in radius values and a 20% change in electron density. Table 3 shows the results of the fitting process.

We note that the Strömgen sphere model assumes a uniform density structure. The spherical and cylindrical cases in the Olzon models likewise adopt uniform density, which explains the small differences between them. Since our sources were not spatially resolved and the power-law models require more observational constraints, we adopted the spherical distribution as the most practical approach.

4.2 Spherical Stellar Wind

According to an alternative scenario proposed by Rodríguez et al. [2012], the free-free emission may originate from a spherical (isotropic) stellar wind. Equation (1) relates the flux density to the frequency, mass-loss rate, terminal velocity V_∞ and distance. The equation is attributed to Panagia and Felli [1975] and Felli and Panagia [1981], and assumes a temperature of 10^4 K for the ionized gas and a mean atomic weight per electron of 1.2.

$$\left[\frac{S_\nu}{\text{mJy}} \right] = 1.28 \left[\frac{\nu}{\text{GHz}} \right]^{0.6} \left[\frac{\dot{M}}{10^{-5} M_\odot \text{ yr}^{-1}} \right]^{4/3} \times \left[\frac{V_\infty}{10^3 \text{ km s}^{-1}} \right]^{-4/3} \left[\frac{D}{\text{kpc}} \right]^{-2} \quad (1)$$

Adopting a typical terminal velocity of 10^3 km s⁻¹ [Rodríguez and Canto, 1983] and using the 6 cm flux densities reported in Table 2, we can calculate the corresponding mass loss rates. These

values are reported in column 2 of Table 4.

Additionally, the minimum number of Lyman-continuum photons needed to ionize the envelope N_c was derived by Felli and Panagia [1981] and is given by equation 2.

$$\begin{aligned} \left[\frac{N_c}{\text{s}^{-1}} \right] &= 2.9 \times 10^{47} \left[\frac{\dot{M}}{10^{-5} M_\odot \text{ yr}^{-1}} \right]^2 \left[\frac{V_\infty}{10^3 \text{ km s}^{-1}} \right]^{-2} \\ &\times \left[\frac{R}{10 R_\odot} \right]^{-1} \end{aligned} \quad (2)$$

To estimate the maximum mass loss rate for zero-age main-sequence (ZAMS) stars, we use equation 2, replacing N_c with the closest value of ionizing photon rate (N_i) and radius (R) from Panagia [1973] and adopt a terminal velocity of 1000 km s⁻¹. The resulting mass loss rates are shown in column 5 of Table 4. We also included the luminosity from Panagia [1973] and the infrared luminosity from Table 1 in Table 4. Except for two sources, G48.99–0.30 and G53.04+0.11se, the IR luminosity from Table 1 and the luminosity of a similar ZAMS star are within a factor of 3 of one another. Thus, except for these two cases, a spherical stellar wind is a plausible model. For the two exceptions, the large luminosity excess reported in Table 4 cannot be explained by the corresponding stellar spectral type.

4.3 Collimated Stellar Wind (Jet)

An alternative to the spherical wind model is the case of a collimated wind or jet. In this case, the mass loss rate can be estimated using the results of Reynolds [1986].

$$\begin{aligned} \left[\frac{\dot{M}}{10^{-6} M_\odot \text{ yr}^{-1}} \right] &= 0.938 \chi_0^{-1} \left[\frac{\mu}{m_p} \right] \left[\frac{V_w}{10^3 \text{ km s}^{-1}} \right] \left[\frac{S_\nu}{\text{mJy}} \right]^{3/4} \\ &\times \left[\frac{\nu}{10 \text{ GHz}} \right]^{-3\alpha_{op}/4} \left[\frac{D}{\text{kpc}} \right]^{3/2} \\ &\times \left[\frac{\nu_m}{10 \text{ GHz}} \right]^{-0.45+3\alpha_{op}/4} [\tan \theta_0]^{3/4} \\ &\times \left[\frac{T}{10^4 \text{ K}} \right]^{-0.075} [\sin i]^{-1/4} \\ &\times \left[\frac{2.1(\alpha_{op} - 1.3)}{(\alpha_{op} - 2)(\alpha_{op} + 0.1)} \right]^{-3/4} \end{aligned} \quad (3)$$

Here, $\chi_0 = 1$ represents the ionized fraction of hydrogen, μ is mean particle mass per hydrogen atom, m_p is the proton mass and is assumed to be $\frac{\mu}{m_p} = 1$. V_w is the collimated wind velocity, S_ν is density flux at $\nu=5$ GHz, $T=10^4$ K, D is the distance to region from Table 1, ν_m is the turnover frequency and α_{op} is the opaque spectral index. The turnover frequencies were taken as 10 GHz for all sources, except for G40.28–0.22 where we used 20 GHz. The opaque spectral index α_{op} was determined between 6 and 8 GHz. However, for the sources G34.82+0.35 and 40.28–0.22, the opaque spectral index was taken from Table 2 because the fluxes at 8 GHz appear to be affected by extended emission, due to the larger beam size at that frequency. We calculate the jet mass loss rate for two (arbitrarily chosen but reasonable) cases: one with $i=45^\circ$ and $\theta_0=27^\circ$, the other with $i=25^\circ$ and $\theta_0=10^\circ$. Here i represents the inclination angle of the jet with respect to the sky while θ_0 is the jet opening angle. These mass loss rates are presented in Table 5.

5 NOTES ON INDIVIDUAL SOURCES

In this section we present the detailed results and discussion for the five individual fields we observed. The sources are all massive young stellar objects embedded in molecular clumps, whose temperatures were determined by ammonia observations of [Cyganowski et al. \[2013\]](#) and masses from ATLASGAL continuum observations of [Urquhart et al. \[2011\]](#). The clump temperatures range from 19 to 31 K, while the clump masses range from 215 to 12300 M_{\odot} (Table 6). For each source we comment on the HII region model and the two stellar wind model results.

5.1 G34.82+0.35

The G34.82+0.35 region, also known as IRAS 18511+0146, Mol75 and RAFGL 5542, was proposed as a candidate precursor to a UC HII region [[Molinari et al., 1996](#)]. [Vig et al. \[2007\]](#) presented an extensive analysis and suggested that IRAS 18511+0146 is a protocluster with the most massive member being a precursor to a Herbig Ae/Be star. They presented 450 and 850 μm images of a dusty molecular region about 1' in size that showed evidence of internal structure. Their MIPS images at 70 and 24 μm resolved the region into three distinct sources. The brighter two of these, A and B, were considered active star formation sites, owing to the presence of water and methanol masers in their vicinity ([Urquhart et al. \[2011, 22 GHz\]](#), [Kurtz et al. \[2004, 44 GHz\]](#), [Pandian et al. \[2009, 6.7 GHz\]](#) and [Fontani et al. \[2010, 6.7 GHz\]](#)). In addition, [Zhang et al. \[2005\]](#) report a molecular outflow in the region, which they detected in the CO(2-1) line.

We find two radio continuum sources: G34.82+0.35w, corresponding to Source A from [Vig et al. \[2007\]](#), and G34.82+0.35e, corresponding to their Source B (see Fig. 1). The angular separation between the two is 21'', corresponding to a projected distance of 0.37 pc. G34.82+0.35w (source A), was detected at 3.6 cm by [Watt and Mundy \[1999\]](#). Their image also shows weak 3.6 cm emission at the position of G34.82+0.35e (source B) but they do not report it as a detection. In our observations, both sources are unresolved at 2 cm and marginally resolved at 6 cm. G34.82+0.35e was detected by [Sánchez-Monge et al. \[2011\]](#) at 1.3 and 3.6 cm, while G34.82+0.35w was marginally detected at 3.6 cm and not detected at 1.3 cm. Both sources are shown in Figure 1.

The salient aspect of the two sources is that G34.82+0.35w is IR-loud and radio-quiet, while G34.82+0.35e is the reverse; see [Vig et al. \[2007\]](#). Both sources are embedded within the same molecular cloud, which both [Vig et al. \[2007\]](#) and [Watt and Mundy \[1999\]](#) estimate to have a mass of order $10^3 M_{\odot}$; the former based on 450/850 μm observations, the latter on CO observations. Thus, the two sources appear to be distinct massive star formation sites within a single molecular core; their different behavior in terms of radio versus infrared emission perhaps indicating different stages of development.

[Vig et al. \[2007\]](#) estimate that G34.82+0.35e is ionized by a B2-B1 star, with a Lyman photon flux of $\sim 1.3 \times 10^{45} \text{ s}^{-1}$, in close agreement with our spherical HII region estimate of $1.0 \times 10^{45} \text{ s}^{-1}$. Their bolometric luminosity of 4400 L_{\odot} is also in good agreement with our HII region model estimate of 5000 L_{\odot} , also indicative of a B1 type star. This close agreement suggests that a single star may be exciting the G34.82+0.35e region. That G35.82+0.35w is weaker in radio, but substantially brighter in the infrared, suggests that multiple protostars, of lower mass, are powering this region.

Considering the spectral indices of 0.4 and 0.6, the small sizes of both sources, and their luminosities obtained via the ionizing photon rate (0.29 and $0.50 \times 10^4 L_{\odot}$) which are less than the total infrared luminosity of the region ($2 \times 10^4 L_{\odot}$), we consider that these sources may be small and weak UC HII regions. However, the radio continuum properties are not exclusive of stellar winds or jets, and we cannot rule out these possibilities.

5.2 G40.28–0.22

G40.28–0.22 is associated with IRAS 19031+0621, which is embedded in an infrared dark cloud (IRDC) [Peretto and Fuller, 2009, Cyganowski et al., 2008] and has been classified as an Extended Green Object (EGO) (see Figure 2) and a candidate Massive Young Stellar Object (MYSO) [Cyganowski et al., 2008]. Both the Bolocam Galactic Plane Survey [Rosolowsky et al., 2010] and the ATLASGAL Survey [Csengeri et al., 2014] report a dusty cloud, surrounding the radio continuum source. Class I and II methanol masers and water masers are reported by Chen et al. [2011], Pandian et al. [2009], and Cyganowski et al. [2013], respectively. Pandian et al. [2010] detected 1.3 cm and 6.9 mm continuum emission coincident with the 6.7 GHz methanol maser. Their results suggest that the 6.9 mm emission has a strong contribution from dust, thus we do not include this point in our modeling of the radio free-free emission.

Sánchez-Monge et al. [2011] report a single unresolved source at 3.6 cm and 1.3 cm with an estimated size between 1 and 10 mpc and an emission measure of $\gtrsim 10^9$ pc cm $^{-6}$. We detect the continuum source at both wavelengths (6 and 2 cm) as shown in Figure 1, where we also show the re-processed 1.3 and 3.6 cm images. In Figure 2 we show the infrared emission, exhibiting the EGO characteristics.

The fit results (Figure 3, Table 3), indicate that the source is small, with a radius of ~ 66 AU (0.32 mpc) with a high density (2.4×10^6 cm $^{-3}$) and an emission measure of 3.7×10^9 pc cm $^{-6}$. The Lyman photon flux corresponds to a single ZAMS B1 star. Ge et al. [2014] reported that the EGO cloud core has a size of 52 mpc, a mass of $25 M_{\odot}$, and a density of 5.53×10^6 cm $^{-3}$. We note the general agreement between the reported molecular core density and the ionized gas density.

In summary, considering the spectral index of 1.64 (between 5 and 22 GHz) as well as the small size, high density, and emission measure, the source meets the usual criteria for a HC HII region [Kurtz, 2002, 2005]. If the source were a stellar wind the radio emission would imply a mass loss rate of about $10^{-5} M_{\odot}$ year $^{-1}$ corresponding to a stellar luminosity of $3.8 \times 10^4 L_{\odot}$ (see Table 4), nearly a factor of 2 higher than the region’s reported IR luminosity of $2.13 \times 10^4 L_{\odot}$.

To our knowledge, there is no evidence in the literature for the presence of an outflow in this region, and the radio continuum morphology has yet to be spatially resolved. We consider this source to be a prime candidate for detailed studies of HC HII regions.

5.3 G48.99-0.30

This region is part of the W51B complex [Koo, 1999] and is associated with IRAS 19201+1400. A continuum source was reported by the CORNISH survey [Hoare et al., 2012] at 6 cm, coincident with IR emission. The Sánchez-Monge et al. [2011] data show a point source to the north of a possible bright rim (see Fig. 1). Although several surveys in the infrared and radio continuum have included this region (RMS, CORNISH, ATLASGAL, and HI-GAL), the compact source has not been well-studied. Water [Nagayama et al., 2015] and methanol [Pandian et al., 2009] masers were found near the centimeter source. [Nagayama et al., 2015] report a distance of $5.62_{-0.49}^{+0.59}$ kpc based on VERA parallax observations of the water masers.

As noted by Sánchez-Monge et al. [2011], extended emission is present in the field. To suppress the resulting imaging artifacts, we used only visibilities from baselines longer than 20 k λ , corresponding to a largest angular size of 6 $''$. We detected the point source, G48.99–0.30, at 6 and 2 cm wavelengths, as shown in Figure 1 (along with the re-processed data at 1.3 and 3.6 cm). An infrared image is shown in Figure 2, where the bright rim is clearly visible. The source is associated with the most massive ($12,000 M_{\odot}$) and hottest (27.6 K) clump among the four detected within the IRDC by Traficante et al. [2015].

Our fitting procedure for an HII region (Table 3) indicates that the source is quite small (3.7 mpc), of high density ($2.3 \times 10^5 \text{ cm}^{-3}$) and emission measure ($3 \times 10^8 \text{ pc cm}^{-6}$). These results and the spectral index (+0.48) suggest that the source could be a HC HII region. The Lyman photon flux could be provided by a single ZAMS-type B0.5 star, which would have a bolometric luminosity of about $1.1 \times 10^4 L_{\odot}$ — somewhat lower than the IR luminosity of $4.5 \times 10^4 L_{\odot}$ reported by Maud et al. [2015].

Our analysis of the stellar wind scenario (Table 4) indicates that this model is not viable because the stellar bolometric luminosity inferred from the ionizing photon rate would be $15 \times$ higher than the IR luminosity of the region. Similarly, the jet scenario (Table 5) is unlikely because the predicted mass-loss rate of $3.9 \times 10^{-4} M_{\odot} \text{ year}^{-1}$ is extremely high.

5.4 G53.04+0.11

This region is associated to IRAS 19266+1745, located at 9.4 kpc (Table 1) with an IR luminosity of $5 \times 10^4 L_{\odot}$ [Lu et al., 2014]. It is associated with a massive clump detected at submillimeter wavelengths [Urquhart et al., 2014, Williams et al., 2004] with a mass between 1300 and 2800 M_{\odot} . A massive outflow, seen in CO, was reported by Beuther et al. [2002b].

Only one continuum source was reported by Sánchez-Monge et al. [2011], detected at both 3.6 cm and 1.3 cm with flux densities of 1.8 and 2.5 mJy, respectively. The RMS survey detected this source at 6 cm with a flux density of 1.1 mJy (beam $\sim 0.7''$) [Urquhart et al., 2009] and it was marginally detected (3-4 σ) in the 6 cm CORNISH survey [Hoare et al., 2012]. Weak water, class II and class I methanol masers were reported by Sridharan et al. [2002], Pandian et al. [2009] and Litovchenko et al. [2011].

After re-calibrating the data at 3.6 and 1.3 cm, we detect two sources (Figure 1). The more southern source is brighter, and coincides with the source reported by Sánchez-Monge et al. [2011] and Urquhart et al. [2009]. The more northern (and western) source is fainter and is detected at 3.6 cm but not at 1.3 cm.

In our new observations at 6 and 2 cm we detect both the northern and southern sources, and we resolve the southern source into two components. We label these three as G53.04+0.11nw, G53.04+0.11se and G53.04+0.11sw (see figure 1). The separation between G53.04+0.11nw and the southern sources is $\sim 9.5''$ while G53.04+0.11sw is found $2.4''$ west of G53.04+0.11se. The latter is the brightest of the three sources while G53.04+0.11sw is the faintest. All three sources are unresolved at our resolution; their flux densities are listed in Table 2.

G53.04+0.11se at 6 cm and 2 cm corresponds to the 1.3 and 3.6 cm continuum source at reported by Sánchez-Monge et al. [2011], but with a lower angular resolution ($7''$). With our better resolution of $0.9''$ and $3''$ at 2 and 6 cm, respectively, we resolve this source into two components which we label as se and sw. In addition, with our better sensitivity we detect the nw source, which is also evident in the re-imaged data at 3.6 cm. Flux densities for the three components are reported in Table 2.

The sw and se sources lie at the edge of extended IR emission as seen in the GLIMPSE data. The nw source is coincident with an IR point source, also seen in the GLIMPSE images (see Fig. 2).

More recently, IRAS 19266+1745 was observed by Rosero et al. [2016] at 6 and 1.3 cm and by Rodríguez et al. [2023] at 7 mm. Our sources G53.04+0.11se and G53.04+0.11sw are associated with the continuum sources A and B, respectively, as reported by Rosero et al. [2016]. Their source C is located further to the south and is not reported by us, while our source G53.04+0.11nw is not reported by them. Rodríguez et al. [2023] report 7 mm continuum emission in sources C1, C3, and C5 (corresponding to se, sw and nw in our nomenclature). In all three cases, their flux densities

appear to be dominated by dust emission; we do not consider them in our analysis.

We obtained flat to positive spectral indices for the three sources G53.04+0.11se ($\alpha=0.12$), G53.04+0.11sw ($\alpha=0.71$), and G53.04+0.11nw ($\alpha=0.42$), which are consistent with thermal emission in HII regions. However, this is inconsistent with the findings of Rosero et al. [2016] for their sources A and B (se and sw in our nomenclature). Although our 6 and 3.6 cm fluxes are in reasonable agreement with their two 6 cm values (at 4.9 and 7.4 GHz), our 2 and 1.3 cm fluxes are notably higher than their two 1.3 cm values (at 20.9 and 25.5 GHz). As a result, we obtain substantially more positive spectral indices than they report. Possible reasons for this discrepancy include differences in the data reduction and variability in the region. Because both sources show a similar increase in flux density with respect to the Rosero et al. [2016] values, we suspect that differing data reduction procedures are the more likely cause.

Our observations and spherical modelling suggest that all three sources are very small (2-6 mpc from model fits). The densities and emission measures are of similar order of magnitude (10^5 cm^{-3} and 10^8 pc cm^{-6}) and the ionizing star of each is likely a B0.5-type ZAMS star, assuming that each ionized region has only one embedded star. Although the size is quite small, the density is not really high enough to consider these as hypercompact HII regions. If the photoionized Strömgen sphere model holds, then the physical interpretation would be that these are small and rather weak UC HII regions.

G53.04+0.11sw could be a stellar wind with a mass loss rate of $2.2 \times 10^{-5} M_{\odot} \text{ yr}^{-1}$, corresponding to a luminosity of $6.5 \times 10^4 L_{\odot}$. This is slightly larger than the luminosity of the region ($5 \times 10^4 L_{\odot}$). We cannot conclusively distinguish between a stellar wind and a UC HII region because the luminosity of the region is roughly consistent with both scenarios.

It is unlikely that G53.04+0.11se is a stellar wind (Table 4), as the luminosity corresponding to its mass loss rate appears is much higher than the luminosity of the region (39.8 versus $5 \times 10^4 L_{\odot}$). Additionally, it is unlikely that these three sources are jets because there was no detection of SiO(1-0) emission [Zapata et al., 2009], which is a tracer of molecular flows. We note that the IR luminosity reported in Tables 1 and 5 is based on *IRAS* data, and hence is the total luminosity of the region, not that of the individual components.

5.5 G53.14+0.07

We detected three continuum sources (G53.14+0.07se, G53.14+0.07sw, G53.14+0.07n) at 2 cm. They are arranged in a triangle, with G53.14+0.07n located at the apex, about 4'' north of the other two sources (see Figure 1). We did not detect the southern sources at 6 cm with an rms of $40 \mu\text{Jy beam}^{-1}$, and they were not detected by Sánchez-Monge et al. [2011] at 3.6 cm, who report a single source at 1.3 cm. Our re-reduced image of their 1.3 cm data shows extended, diffuse emission to the south of G53.14+0.07n, which may have a contribution from the two southern sources. At 2 cm, G53.14+0.07sw is slightly elongated in the east-west direction and has the highest flux density ($S_{2\text{cm}} = 0.3 \text{ mJy}$) of the three sources (see Table 2). G53.14+0.07se and G53.14+0.07n are unresolved and have flux densities of approximately 0.16 mJy.

All three sources we detect are coincident with the MM1 core of the G053.11+0.05 IRDC reported by Rathborne et al. [2006]. MM1 is the most massive core within the IRDC, with a mass of $124 M_{\odot}$ based on 1.2 mm observations. The source is associated with infrared emission, class I and II methanol masers, and water masers (see Figure 2 and Table 4).

G53.14+0.07n coincides with YSO1 reported by Kim et al. [2018], while G53.14+0.07sw is within several arc seconds of their position for YSO2. They report a molecular outflow, detected in H_2 , and suggest that one of the two YSOs is the driving source. The elongated morphology of G53.14+0.07sw, although not well-aligned with the outflow, suggests that it may be the outflow

driver.

We could not use the Olon models for these sources as for the other regions, owing to a reliable flux density at only one frequency. However, we were able to estimate an upper limit for their size of about 10 mpc. We can then apply the standard equations for a spherical, homogeneous, isothermal HII region (with an assumed electron temperature of 10^4 K) and also for the spherical wind scenario, described in Section 4.2.

The calculated properties of the three sources are consistent with small UC HII regions, whose Lyman continuum photon flux ($\sim 10^{43}$ s $^{-1}$) corresponds to a ZAMS B3 or B2 star [Panagia, 1973]. More massive stars are possible, because the sizes reported in Table 2 are upper limits. These regions might also be stellar winds. The luminosities (Table 4) would be slightly higher than that of the region, but only by factors of a few, which is within the uncertainty.

6 Discussion and conclusions

The simplest model for a HC HII region is a Strömgren sphere within a very high density medium and with an abundant supply of ionizing photons. However, as several decades of research have shown, and as alluded to in the introduction and Section 4.1, the simplicity of this model fails to address numerous aspects of these regions. Mass infall and outflow, along with circumstellar accretion disks, substantially complicate the dynamics of HII regions; this is just as much the case for hypercompact regions as it is for their larger and lower density cousins, the compact and ultracompact HII regions.

The observed source sizes from the radio continuum for our sample of candidate HC HII regions are quite small, even for hypercompact regions (see Table 2). Nevertheless, the electron densities (assuming the spherical Olon model, see Table 3), although fairly high for UC HII regions, are somewhat on the low side for HC HII regions. Perhaps most notable from our modeling is that — at these size scales — cylindrical, spherical and Gaussian distributions predict very similar continuum spectra. It would appear that only highly-resolved images will be able to distinguish the true density profile.

We investigated five candidate HC HII regions that were previously observed at 1.3 and 3.6 cm. To expand on those observations, we conducted new observations at 2 and 6 cm using the VLA and detected a total of 10 compact sources in these five regions. Of these sources, five are newly detected, as three of the original sources were resolved into multiple components. The observed source radii are in the range of 4 to 10 mpc. Using the spherical Olon model and the source flux density distributions, the model radii are smaller, ranging from 0.4 to 3.7 mpc. Using a spherical stellar wind model, the mass loss rates range from 0.17 to 15.9×10^{-5} M_{\odot} yr $^{-1}$.

Of the 10 sources we report, we favor the interpretation of a HC HII region for two of them, G40.28–0.22 and G48.99–0.30. These sources are particularly good candidates for further HC HII region studies. For the remaining eight sources we consider small, weak UC HII regions to be the more likely interpretation. For five of these (the two components of G34.82+0.35 and the three components of G53.14+0.07) we cannot rule out either the spherical wind or the jet interpretation. One of our top candidates for a jet is G34.82+0.35w. Its spectral index (+0.6) and mass loss rate (between 5 and 9×10^{-6} M_{\odot} yr $^{-1}$) are reasonable for a jet. In addition, it is associated with an outflow reported in CO (J=2-1) [Zhang et al., 2005] and methanol masers that may have formed in gas shocked by the flows. For the remaining three sources, of G53.04+0.11, the sw source could be a wind, but the se source is unlikely to be, based on luminosity arguments. We reject the jet hypothesis for all three sources, based on the lack of shocked gas tracers.

When compared to the size of our solar system, given by the heliopause of about 130 AU or 0.6

mpc, we note that our regions are similar in size to the solar system. In contrast, the stellar density in the core of the Orion Trapezium is approximately 2×10^4 stars pc^{-3} [Hillenbrand and Hartmann, 1998], equivalent to having one star per 40 mpc assuming a uniform stellar distribution in the core. Hence, we believe that the HC HII regions host only one or two stars.

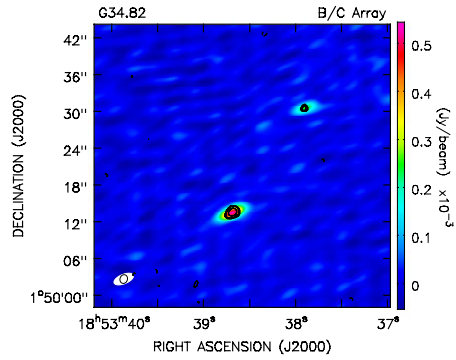
In summary, our observations and modeling indicate that most sources are best classified as small, weak UC HII regions, although a few remain viable candidates for HC HII regions. One source, G34.82+0.35w, is a strong jet candidate. Future multi-wavelength observations with higher angular resolution will be essential to resolve these sources and confirm their nature.

Acknowledgements

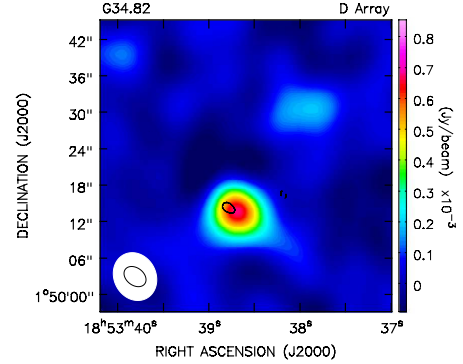
We thank the anonymous referee for helpful suggestions and comments that improved the quality of the paper.

A.S.-M. acknowledges support from the RyC2021-032892-I grant funded by MCIN/AEI/10.13039/501100011033 and by the European Union ‘Next GenerationEU’/PRTR, as well as the program Unidad de Excelencia María de Maeztu CEX2020-001058-M, and support from the PID2023-146675NB-I00 (MCI-AEI-FEDER, UE).

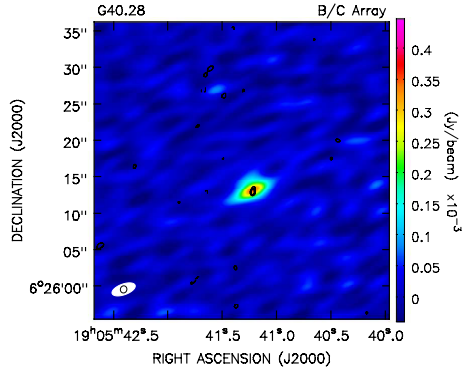
T.R.E. is grateful to The World Academy of Science (TWAS) for a postdoctoral grant during which most of this work was completed.



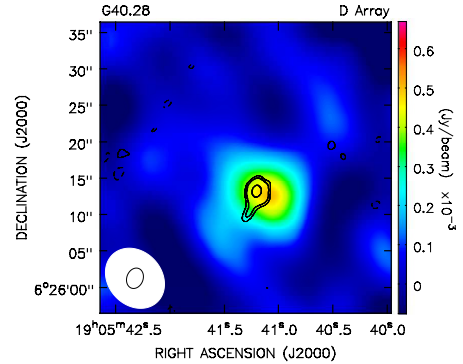
(a) G34.82+0.35 (2 y 6 cm)



(b) G34.82+0.35 (1.3 y 3.6 cm)

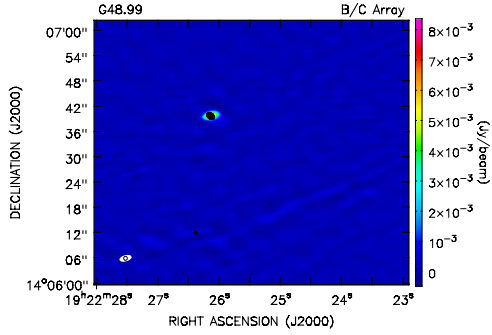


(c) G40.28-0.22 (2 y 6 cm)

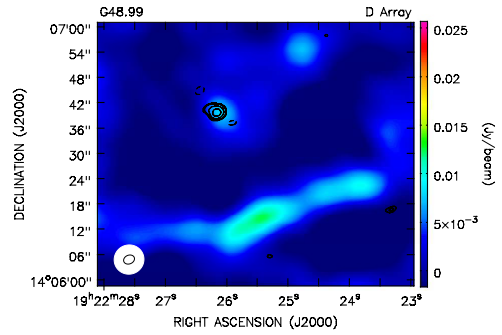


(d) G40.28-0.22 (1.3 y 3.6 cm)

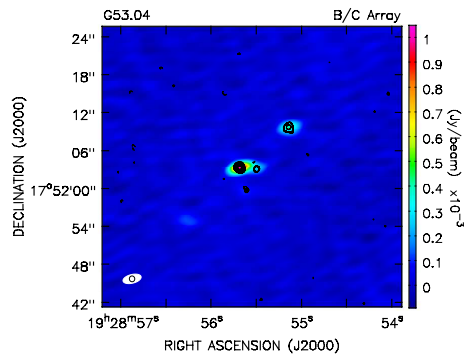
Figure 1: Radio continuum images. Left: color map of the 2 cm emission (VLA-C) overlaid with contours of the 6 cm emission (VLA-B). Right: color map of the 3.6 cm emission (VLA-D) overlaid with contours of the 1.3 cm emission (VLA-D). The contour levels are $-3, 3, 2^n \dots 32$, $n=2 \dots 5$ of the map rms given in Table 1. The synthesized beams are shown in the bottom-left corner of each map.



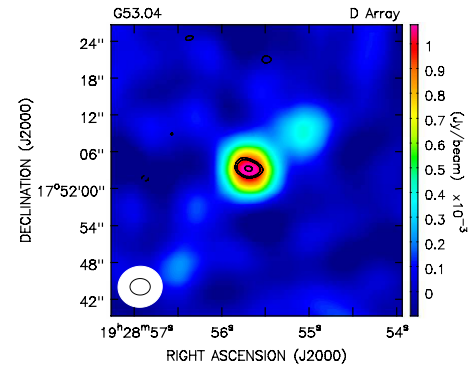
(e) G48.99-0.30 (2 y 6 cm)



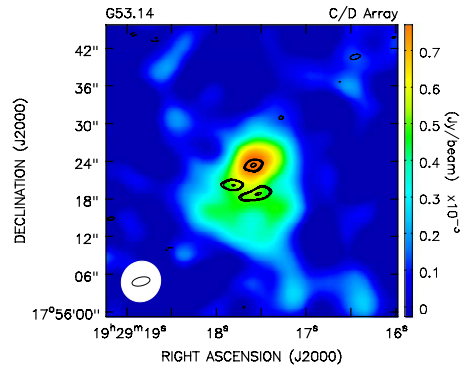
(f) G48.99-0.30 (1.3 y 3.6 cm)



(g) G53.04+0.11 (2 y 6 cm)

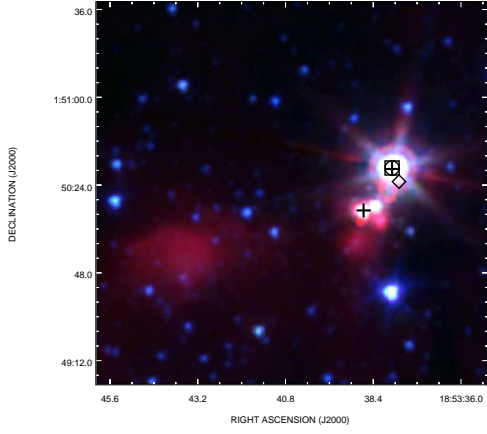


(h) G53.04+0.11 (1.3 y 3.6 cm)

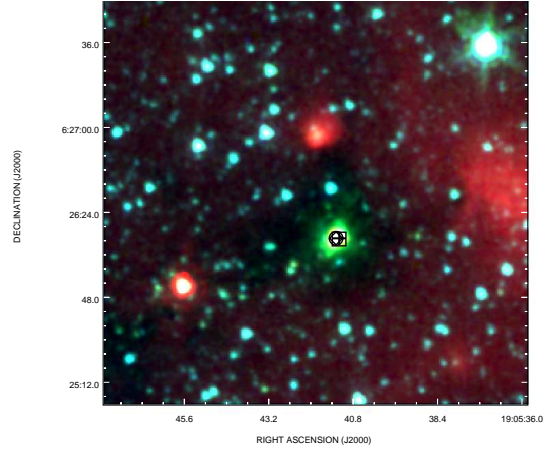


(i) G53.14+0.07 (1.3 y 2 cm)

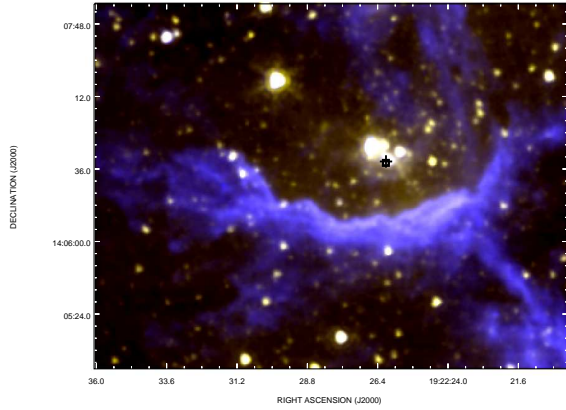
Figure 1: Cont.Radio continuum images. For G53.14+0.07, the 1.3 cm emission (VLA-D) color image is overlaid with a contour map of the 2 cm emission (VLA-C).



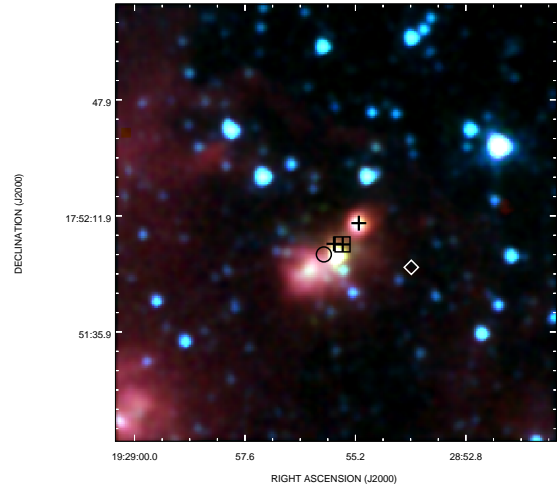
(a) G34.82+0.35



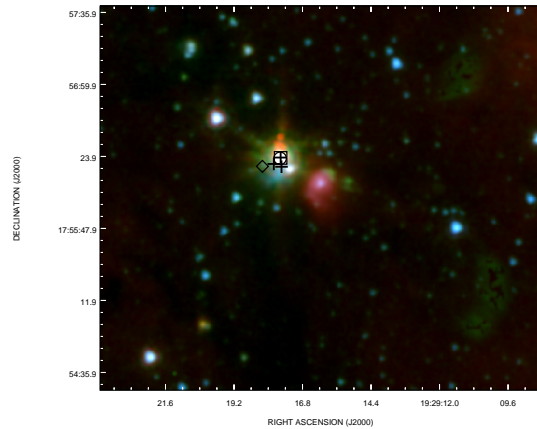
(b) G40.28-0.22



(c) G48.99-0.30



(d) G53.04+0.11



(e) G53.14+0.07

Figure 2: Overlay of infrared emission at $8.0 \mu\text{m}$ (red), $4.5 \mu\text{m}$ (green), and $3.6 \mu\text{m}$ (blue) taken from the GLIMPSE IRAC images [Churchwell and GLIMPSE Team, 2001, Benjamin et al., 2003]. The radio sources we detect are marked with crosses. The positions of class I and class II methanol masers are indicated by diamonds and squares, respectively, and the positions of water masers are indicated by circles. References for each tracer are listed in Table 7.

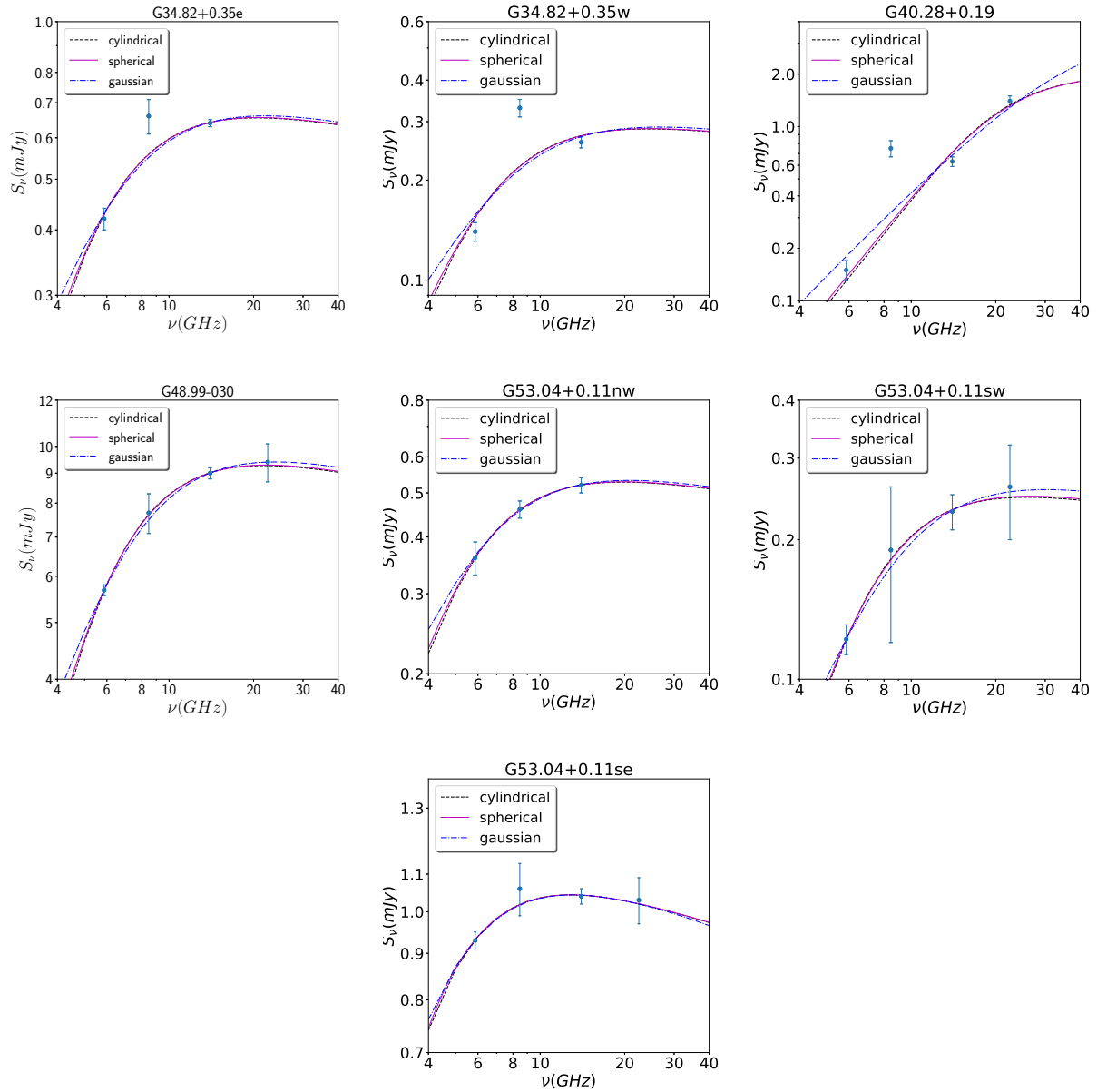


Figure 3: Radio continuum spectra. The points correspond to the observations. Models are shown with a dashed line (cylindrical distribution), solid line (spherical distribution), and dot-dashed line (Gaussian distribution).

Table 1: Source Properties and Observing Parameters.

Source	IRAS Name	pointing center ^a		Phase calibrator	6 cm		3.6 cm		2 cm		1.3 cm		D ^c kpc	L ^d 10 ⁴ L _⊙ (kpc)
		α(J2000.0)	δ(J2000.0)		beam (")	rms mJy beam ⁻¹	beam ^b (")	rms mJy beam ⁻¹	beam (")	rms mJy beam ⁻¹	beam ^b (")	rms mJy beam ⁻¹		
G34.82+0.35	18511+0146	18 53 37.90	01 50 30.0	J1851+0035	1.02×0.91	0.03	8.46×7.28	0.05	3.38×1.52	0.02	3.75×2.93	0.20	3.6	2.01 (3.86)
G40.28−0.22	19031+0621	19 05 41.22	06 26 12.7	J1851+0035	0.99×0.89	0.03	8.95×7.34	0.05	3.35×1.47	0.02	2.87×2.23	0.08	4.9	2.13 (4.91)
G48.99−0.30	19201+1400	19 22 26.13	14 06 39.8	J1922+1530	0.94×0.86	0.6	7.18×6.91	2.0	2.93×1.39	0.25	2.66×2.06	0.30	5.1	4.5 (5.4)
G53.04+0.11	19266+1745	19 28 55.60	17 52 03.0	J1922+1530	0.92×0.85	0.02	7.22×6.69	0.06	2.93×1.37	0.02	3.66×2.44	0.13	9.4	5.0 (9.5)
G53.14+0.07	19270+1750	19 29 17.58	17 56 23.2	J1922+1530	0.91×0.86	0.02	9.82×7.21	0.12	2.91×1.36	0.02	6.56×6.17	0.13	1.9	0.44 (1.8)

^a Units of right ascension are hours, minutes, and seconds, and units of declination are degrees, arcminutes, and arcseconds.

^b Beam sizes are from our re-analysis of the [Sánchez-Monge et al. \[2011\]](#) data.

^c Distances from [Pandian et al. \[2009\]](#), based on methanol masers detected in these regions.

^d Infrared Luminosity from [Zhang et al. \[2001\]](#), [Traficante et al. \[2015\]](#), [Maud et al. \[2015\]](#), [Lu et al. \[2014\]](#), [Rathborne et al. \[2010\]](#). In parentheses we give the distances used to obtain the luminosities.

Table 2: Observed Parameters of the Continuum Emission.

Source	Peak Position ^a		S_{6cm}^b (mJy)	$S_{3.6cm}$ (mJy)	S_{2cm} (mJy)	$S_{1.3cm}$ (mJy)	Size ^c "	R ^d AU	R ^d mpc	Spectral Index	T _b ^e K
	α (J2000.0)	δ (J2000.0)									
G34.82+0.35w	18 53 37.9	01 50 30.6	0.14±0.01	0.33±0.02	0.26±0.01	<1.0	≲0.51 ×0.46	900	4	0.6±0.4	>24
G34.82+0.35e	18 53 38.68	01 50 13.6	0.42±0.02	0.66±0.05	0.64±0.01	<1.0	≲0.51 ×0.46	900	4	0.4±0.2	>73
G40.28−0.22	19 05 41.21	06 26 13.0	0.15±0.08	0.75±0.07	0.63±0.04	1.4±0.2	≲0.49×0.45	1200	6	1.64±0.07	>42
G48.99−0.30	19 22 26.13	14 06 39.7	5.68±0.12	7.7±0.6	9.0±0.2	9.4±0.7	≲0.47×0.43	1100	6	0.48±0.07	>1100
G53.04+0.11nw	19 28 55.14	17 52 09.7	0.36±0.03	0.46±0.02	0.52±0.02	<0.36	≲0.46×0.43	2100	10	0.42±0.05	>75
G53.04+0.11sw	19 28 55.49	17 52 03.1	0.12±0.01	0.19±0.07	0.23±0.02	0.26±0.06	≲0.46×0.43	2100	10	0.71±0.07	>25
G53.04+0.11se	19 28 55.68	17 52 03.3	0.93±0.02	1.06±0.07	1.04±0.02	1.03±0.06	≲0.46×0.43	2100	10	0.12±0.03	>190
G53.14+0.07sw ^f	19 29 17.55	17 56 18.8	<0.1	<0.60	0.30±0.05	3.3±0.4 ^g	3.59×1.10	1900	9	-	0.5
G53.14+0.07n ^f	19 29 17.58	17 56 23.4	<0.1	<0.60	0.16±0.01	-	≲1.45×0.68	940	5	-	>1.1
G53.14+0.07se ^f	19 29 17.82	17 56 20.2	<0.1	<0.60	0.17±0.01	-	≲1.45×0.68	940	5	-	>1.2

^a Units of right ascension are hours, minutes, and seconds, and units of declination are degrees, arcminutes, and arcseconds. Positions are obtained from the 6 cm images except for the G53.14+0.07 region for which the 2 cm image was used.

^b The flux density limit for non-detections is set to 3σ , where σ is the rms noise of the maps given in Table 1.

^c We use 6 cm maps to estimate the source sizes. If the sources are unresolved we use half the synthesized beam size. If the sources are resolved we report the size deconvolved from the beam.

^d The radius is estimated as half of the geometric mean of the major and minor axes given in the Size column and using the source distance from Table 1.

^e Brightness temperatures were calculated using the reported source size and 6 cm flux density, except for G53.14+0.07 for which the 2 cm values were used.

^f For this source we use the 2 cm image for the position, size and brightness temperature.

^g Only one source is detected at 1.3 cm owing to the lower angular resolution. The 1.3 cm flux shown for this source is the flux of the more extended region.

Table 3: Calculated parameters using Spherical Olon Model.

Source	R mpc	R AU	R "	Ne 10^5 cm^{-3}	EM 10^8 pc cm^{-6}	τ^a	Mi $10^{-6} M_{\odot}$	Ni $10^{46} \text{ phot s}^{-1}$	logNi	SP ^b	L ^b $10^4 L_{\odot}$
G34.82+0.35w	0.3± 0.1	62	0.02	8 ±4	3.8	2.6,1.2,0.4 ,−	1.7	0.055	44.74	B2	0.29
G34.82+0.35e	0.50± 0.05	100	0.03	5 ±1	2.5	1.8,0.8,0.3,−	6.2	0.10	45.00	B1	0.50
G40.28−0.22	0.32± 0.05	66	0.02	24±10	37	29.1,13.5,4.7,1.7	7.8	0.60	45.78	B0.5	1.10
G48.99−0.30	2.48± 0.01	510	0.10	2.32 ± 0.02	2.7	2.1, 0.9, 0.3, 0.1	369.0	2.63	46.42	B0.5	1.10
G53.04+0.11nw	1.22± 0.01	251	0.03	2.94± 0.02	2.1	1.7, 0.8,0.3,−	55.7	0.50	45.70	B0.5	1.10
G53.04+0.11sw	0.63±0.01	130	0.01	5.5±0.1	3.8	3.0,1.4,0.5,0.2	14.2	0.24	45.38	B1	0.50
G53.04+0.11se	2.6 ±0.1	536	0.058	1.3± 0.07	0.88	0.7,0.3,0.1,0.04	244.5	0.95	45.98	B0.5	1.10

^a τ calculated from the spherical model for each wavelength (C, X, U, K) with detection (see Table 2).

^b Spectral type (SP) and luminosity (L) based on $\log N_i$ from Panagia [1973].

Table 4: Mass loss rate for the spherical stellar wind model.

Sources	\dot{M}^a $10^{-5}M_{\odot} \text{ yr}^{-1}$	N_i^b phot.s $^{-1}$	Radius b R_{\odot}	\dot{M}_*^c $10^{-5}M_{\odot} \text{ yr}^{-1}$	L b $10^4 L_{\odot}$	L d $10^4 L_{\odot}$
G34.82+0.35w	0.59	2.3×10^{47}	5.5	0.66	2.5	2.0
G34.82+0.35e	1.33	6.9×10^{47}	6.0	1.20	3.8	2.0
G40.28−0.22	0.98	6.9×10^{47}	6.0	1.20	3.8	2.13
G48.99−0.30	15.9	4.2×10^{49}	12.6	13.5	67.6	4.5
G53.04+0.11nw	5.02	6.6×10^{48}	8.1	4.3	14.8	5
G53.04+0.11sw	2.22	2.2×10^{47}	6.5	2.2	6.5	5
G53.04+0.11se	10.2	2.3×10^{49}	10.7	9.2	39.8	5
G53.14+0.07sw	0.26	1.7×10^{46}	5.1	0.17	1.1	0.44
G53.14+0.07n	0.16	1.7×10^{46}	5.1	0.17	1.1	0.44
G53.14+0.07se	0.17	1.7×10^{46}	5.1	0.17	1.1	0.44

^a Mass loss rate (\dot{M}) determined from equation 1, using the flux density at 5.868 GHz (Table 2); distances are from Table 1; the terminal velocity is 1000 km s $^{-1}$. For G53.14+0.07 the 2 cm (14.5 GHz) flux density was used.

^b Ionizing photon rate (N_i), radius (R_{\odot}) and luminosity (L) from Panagia [1973].

^c Maximum mass loss rate (\dot{M}_*) determined from equation 2, using N_i and R from Panagia [1973] and a terminal velocity of 1000 km s $^{-1}$.

^d Infrared luminosity (L) from Table 1.

Table 5: Mass loss rate for Jet

Sources	\dot{M}_c^a	\dot{M}_c^a	α_{op}^b
	$10^{-6} M_{\odot} \text{ yr}^{-1}$ $i=45^{\circ}$ and $\theta=27^{\circ}$	$10^{-6} M_{\odot} \text{ yr}^{-1}$ $i=25^{\circ}$ and $\theta=10^{\circ}$	
G34.82+0.35w	9	5	0.6 ± 0.4
G34.82+0.35e	14	7	0.4 ± 0.3
G40.28−0.22	–	–	1.6 ± 0.1
G48.99−0.30	393	202	0.8 ± 0.1
G53.04+0.11nw	89	46	0.7 ± 0.1
G53.04+0.11sw	295	151	1.2 ± 0.2
G53.04+0.11se	94	48	0.4 ± 0.1

^a Mass loss rate obtained from equation 3.

^b α_{op} is the opaque spectral index.

Table 6: Parameters of clumps associated with the regions^a.

Region	$T_{kin}(\text{NH}_3)$ K	$F_{int}(870 \mu\text{m})$ Jy	Clump Mass M_{\odot}
G34.82+0.35	18.9	13.21	1000
G40.28−0.22	30.8	13.24	4200
G48.99−0.30	27.6	76.70	12000
G53.04+0.11	25.5	4.95	2800
G53.14+0.07	22.6	15.35	220

^a All values are from [Urquhart et al. \[2011, 2014\]](#) except for the kinematic temperature of G40.28−0.22, which is from [Cyganowski et al. \[2013\]](#). The clump masses assume a dust temperature of 20 K.

Table 7: Tracers of star formation in the sample.

Source	EGO ^a	H ₂ O ^b	CH ₃ OH ^c Class II	CH ₃ OH ^d Class I	Spitzer ^e	1.1 mm ^f	Radio Continuum			
							C ^h	X ^g	KU ^h	K ^g
G34.82+0.35w	-	y	y	y	y	y	y	y	y	n
G34.82+0.35e	-	y	y	n	y	y	y	y	y	y
G40.28−0.22	y	y	y	y	y	y	y	y	y	y
G48.99−0.30	-	y	y	-	y	y	y	y	y	y
G53.04+0.11	-	y	y	y	y	y	y	y	y	y
G53.14+0.07	-	y	y	y	y	y	n	n	y	y

^a Extended Green Object (EGO) [Cyganowski et al. \[2008\]](#).

^b H₂O masers [Urquhart et al. \[2011\]](#), [Cyganowski et al. \[2013\]](#), [Nagayama et al. \[2015\]](#), [Sridharan et al. \[2002\]](#).

^c CH₃OH class II masers [Pandian et al. \[2011\]](#), [Szymczak et al. \[2012\]](#), [Sun et al. \[2014\]](#).

^d CH₃OH class I maser [Kurtz et al. \[2004\]](#), [Chen et al. \[2011\]](#), [Litovchenko et al. \[2011\]](#), [Chen et al. \[2012\]](#).

^e Infrared emission [Vig et al. \[2007\]](#), [Cyganowski et al. \[2008\]](#), [Sun et al. \[2014\]](#) and GLIMPSE/MIPSGAL.

^f 1.1 mm emission [Schlingman et al. \[2011\]](#), [Rosolowsky et al. \[2010\]](#), [Beuther et al. \[2002a\]](#).

^g 1.3 and 3.6 cm emission [Sánchez-Monge et al. \[2011\]](#).

^h 2 and 6 cm emission (this work).

A Appendix

HII regions

We applied the models developed by [Olson \[1975\]](#), who assumed ionized hydrogen gas, circular symmetry around the line of sight and uniform electron temperature (T_e). In the Rayleigh-Jeans regime, the total flux can be expressed by

$$S_\nu = \frac{4\pi k T_e \nu^2}{c^2 D^2} \int_0^\infty \rho \left[1 - e^{-\tau_\nu(\rho)}\right] d\rho \quad (4)$$

To calculate the optical depth of the region, we need to know its geometry and distance. One way to do this is to use the parameter ρ , which is the radial distance from the center of the region to a point on its surface, measured in a plane perpendicular to the line of sight. The distance D is the distance from us to the region. The optical depth at a frequency ν is given by $\tau_\nu(\rho) = 0.08235 \times T_e^{-1.35} \nu^{-2.1} E(\rho)$, where T_e is the electron temperature and $E(\rho)$ is the emission measure. The emission measure depends on the electron density profile of the region, and can be written as $E(\rho) = 2 \int_0^\infty n_e^2(r) dz$, where $r^2 = \rho^2 + z^2$ and z is the coordinate along the line of sight. We tested different models for the electron density distribution, such as cylindrical, Gaussian, and spherical, following the method of [Olson \[1975\]](#).

In what follows we adopt the notation introduced by [Olson \[1975\]](#). Specifically, we write p instead of the central optical depth, $\tau_\nu(0) = fE(0)$. Here $f(\nu, T_e)$ is the Altenhoff approximation [[Olson, 1975](#)] for the free-free absorption coefficient, given by

$$f = f(\nu, T_e) = 8.235 \times 10^{-2} \left(\frac{T_e}{\text{K}}\right)^{-1.35} \left(\frac{\nu}{\text{GHz}}\right)^{-2.1} \text{cm}^6 \text{pc}^{-1}. \quad (5)$$

These definitions and approximations are included here to clarify the notation used in the subsequent equations.

The cylindrical distribution.

Following [Olson \[1975\]](#), we assume a cylindrical geometry in which the electron density is constant, $n_e = n_0$, inside a cylinder of radius R and length $2R$, with its axis of symmetry aligned along the line of sight. Outside the cylinder, $n_e = 0$.

$$p = 2n_0^2 R f \quad (6)$$

$$S_\nu = \frac{2\pi k T_e R^2 \nu^2}{C^2 D^2} (1 - e^{-p}) \quad (7)$$

The Gaussian distribution

Following [Olson \[1975\]](#), we adopt spherical symmetry and assume a Gaussian distribution for the electron density, given by

$$n_e(r) = n_0 \exp\left(-\frac{r^2}{2R^2}\right), \quad (8)$$

where n_0 is the central electron density and R characterizes the scale of the distribution.

$$p = n_0^2 R f \sqrt{\pi} \quad (9)$$

$$S_\nu = \frac{2\pi k T_e R^2 \nu^2}{C^2 D^2} [\gamma + \ln p + E_1(p)] \quad (10)$$

Where The function $E_1(p)$ denotes the exponential integral evaluated between p and infinity,

$$E_1(p) = \int_p^\infty \frac{e^{-t}}{t} dt, \quad (11)$$

and γ is the Euler–Mascheroni constant ($\gamma \approx 0.5772$).

The spherical distribution

Following Olzon [1975], we consider a spherical geometry in which the electron density is uniform, $n_e = n_0$, inside a sphere of radius R , and $n_e = 0$ outside the sphere.

$$p = 2n_0^2 R f \quad (12)$$

$$S_\nu = \frac{2\pi k T_e R^2 \nu^2}{C^2 D^2} \left[1 - \frac{2}{p^2} 1 - (p-1)e^{-p} \right] \quad (13)$$

We applied the minimizing function in Python software to find the optimal values for radius and density by fitting the different models to the data using the least-squares method. The equation we used for the fit is $\chi^2 = \sum_i^N \frac{[S_{\nu_i}^{obs} - S_{\nu_i}^{mod}(a)]^2}{\epsilon_i^2}$, where $S_{\nu_i}^{obs}$ represents the observed data, $S_{\nu_i}^{mod}$ is the model, a is the set of parameters that we want to optimize, and ϵ_i is the error in the flux density (see table 2).

References

- Robert A. Benjamin, E. Churchwell, Brian L. Babler, T. M. Bania, Dan P. Clemens, Martin Cohen, John M. Dickey, Rémy Indebetouw, James M. Jackson, Henry A. Kobulnicky, Alex Lazarian, A. P. Marston, John S. Mathis, Marilyn R. Meade, Sara Seager, S. R. Stolovy, C. Watson, Barbara A. Whitney, Michael J. Wolff, and Mark G. Wolfire. GLIMPSE. I. An SIRTf Legacy Project to Map the Inner Galaxy. *PASP*, 115(810):953–964, August 2003. doi: 10.1086/376696.
- H. Beuther, P. Schilke, K. M. Menten, F. Motte, T. K. Sridharan, and F. Wyrowski. High-Mass Protostellar Candidates. II. Density Structure from Dust Continuum and CS Emission. *ApJ*, 566(2):945–965, February 2002a. doi: 10.1086/338334.
- H. Beuther, P. Schilke, T. K. Sridharan, K. M. Menten, C. M. Walmsley, and F. Wyrowski. Massive molecular outflows. *A&A*, 383:892–904, March 2002b. doi: 10.1051/0004-6361:20011808.
- Xi Chen, Simon P. Ellingsen, Zhi-Qiang Shen, Anita Titmarsh, and Cong-Gui Gan. A 95 GHz Class I Methanol Maser Survey Toward Glimpse Extended Green Objects (EGOs). *ApJS*, 196(1):9, September 2011. doi: 10.1088/0067-0049/196/1/9.
- Xi Chen, Simon P. Ellingsen, Jin-Hua He, Ye Xu, Cong-Gui Gan, Zhi-Qiang Shen, Tao An, Yan Sun, and Bing-Gang Ju. A 95 GHz Class I Methanol Maser Survey toward a Sample of GLIMPSE Point Sources Associated with BGPS Clumps. *ApJS*, 200(1):5, May 2012. doi: 10.1088/0067-0049/200/1/5.
- E. Churchwell and GLIMPSE Team. The Galactic Legacy Infrared Mid-Plane Survey Extraordinaire (GLIMPSE). In *American Astronomical Society Meeting Abstracts #198*, volume 198 of *American Astronomical Society Meeting Abstracts*, page 25.04, May 2001.

- T. Csengeri, J. S. Urquhart, F. Schuller, F. Motte, S. Bontemps, F. Wyrowski, K. M. Menten, L. Bronfman, H. Beuther, Th. Henning, L. Testi, A. Zavagno, and M. Walmsley. The ATLASGAL survey: a catalog of dust condensations in the Galactic plane. *A&A*, 565:A75, May 2014. doi: 10.1051/0004-6361/201322434.
- C. J. Cyganowski, B. A. Whitney, E. Holden, E. Braden, C. L. Brogan, E. Churchwell, R. Indebetouw, D. F. Watson, B. L. Babler, R. Benjamin, M. Gomez, M. R. Meade, M. S. Povich, T. P. Robitaille, and C. Watson. A Catalog of Extended Green Objects in the GLIMPSE Survey: A New Sample of Massive Young Stellar Object Outflow Candidates. *AJ*, 136(6):2391–2412, December 2008. doi: 10.1088/0004-6256/136/6/2391.
- C. J. Cyganowski, J. Koda, E. Rosolowsky, S. Towers, J. Donovan Meyer, F. Egusa, R. Momose, and T. P. Robitaille. A Water Maser and NH₃ Survey of GLIMPSE Extended Green Objects. *ApJ*, 764(1):61, February 2013. doi: 10.1088/0004-637X/764/1/61.
- M. Felli and N. Panagia. Free-free emission from extended envelopes. II - The mass loss and the envelope ionization. *A&A*, 102(3):424–430, October 1981.
- F. Fontani, R. Cesaroni, and R. S. Furuya. Class I and Class II methanol masers in high-mass star-forming regions. *A&A*, 517:A56, July 2010. doi: 10.1051/0004-6361/200913679.
- J. Franco, G. Tenorio-Tagle, and P. Bodenheimer. The evolution of HII regions in disk-like clouds. The appearance of neutral high velocity outflows. *RMxAA*, 18:65, September 1989.
- Jose Franco, Guillermo Tenorio-Tagle, and Peter Bodenheimer. On the Formation and Expansion of H II Regions. *ApJ*, 349:126, January 1990. doi: 10.1086/168300.
- José Franco, Stan Kurtz, Peter Hofner, Leonardo Testi, Guillermo García-Segura, and Marco Martos. The Density Structure of Highly Compact H II Regions. *ApJL*, 542(2):L143–L146, October 2000. doi: 10.1086/312938.
- J. X. Ge, J. H. He, X. Chen, and S. Takahashi. Early-stage star-forming cloud cores in Galactic Legacy Infrared Mid-Plane Survey (GLIMPSE) extended green objects (EGOs) as traced by organic species. *MNRAS*, 445(2):1170–1185, December 2014. doi: 10.1093/mnras/stu1758.
- Lynne A. Hillenbrand and Lee W. Hartmann. A Preliminary Study of the Orion Nebula Cluster Structure and Dynamics. *ApJ*, 492(2):540–553, January 1998. doi: 10.1086/305076.
- M. G. Hoare, C. R. Purcell, E. B. Churchwell, P. Diamond, W. D. Cotton, C. J. Chandler, S. Smethurst, S. E. Kurtz, L. G. Mundy, S. M. Dougherty, R. P. Fender, G. A. Fuller, J. M. Jackson, S. T. Garrington, T. R. Gledhill, P. F. Goldsmith, S. L. Lumsden, J. Martí, T. J. T. Moore, T. W. B. Muxlow, R. D. Oudmaijer, J. D. Pandian, J. M. Paredes, D. S. Shepherd, R. E. Spencer, M. A. Thompson, G. Umana, J. S. Urquhart, and A. A. Zijlstra. The Coordinated Radio and Infrared Survey for High-Mass Star Formation (The CORNISH Survey). I. Survey Design. *PASP*, 124(919):939, September 2012. doi: 10.1086/668058.
- David Hollenbach, Doug Johnstone, Susana Lizano, and Frank Shu. Photoevaporation of Disks around Massive Stars and Application to Ultracompact H II Regions. *ApJ*, 428:654, June 1994. doi: 10.1086/174276.
- Richard Ignace and Ed Churchwell. Free-Free Spectral Energy Distributions of Hierarchically Clumped H II Regions. *ApJ*, 610(1):351–360, July 2004. doi: 10.1086/421453.

- Eric Keto. The Formation of Massive Stars by Accretion through Trapped Hypercompact H II Regions. *ApJ*, 599(2):1196–1206, December 2003. doi: 10.1086/379545.
- Hyun-Jeong Kim, Bon-Chul Koo, Tae-Soo Pyo, and Christopher J. Davis. A Parsec-scale Bipolar H₂ Outflow in the Massive Star-forming Infrared Dark Cloud Core MSXDC G053.11+00.05 MM1. *ApJ*, 863(1):74, August 2018. doi: 10.3847/1538-4357/aace9f.
- Bon-Chul Koo. CO Observations of the W51B H II Region Complex. *ApJ*, 518(2):760–768, June 1999. doi: 10.1086/307316.
- S. Kurtz. Ultracompact HII Regions. In P. Crowther, editor, *Hot Star Workshop III: The Earliest Phases of Massive Star Birth*, volume 267 of *Astronomical Society of the Pacific Conference Series*, page 81, October 2002. doi: 10.48550/arXiv.astro-ph/0111351.
- Stan Kurtz. Hypercompact HII regions. In R. Cesaroni, M. Felli, E. Churchwell, and M. Walmsley, editors, *Massive Star Birth: A Crossroads of Astrophysics*, volume 227 of *IAU Symposium*, pages 111–119, January 2005. doi: 10.1017/S1743921305004424.
- Stan Kurtz, Peter Hofner, and Carlos Vargas Álvarez. A Catalog of CH₃OH 7₀₋₆1 A⁺ Maser Sources in Massive Star-forming Regions. *ApJS*, 155(1):149–165, November 2004. doi: 10.1086/423956.
- I. D. Litovchenko, A. V. Alakoz, I. E. Val’Tts, and G. M. Larionov. Search for class I methanol maser emission in various types of objects in the interstellar medium. *Astronomy Reports*, 55(12):1086–1095, December 2011. doi: 10.1134/S1063772911120080.
- S. Lizano. Hypercompact HII Regions. In H. Beuther, H. Linz, and Th. Henning, editors, *Massive Star Formation: Observations Confront Theory*, volume 387 of *Astronomical Society of the Pacific Conference Series*, page 232, May 2008.
- Susana Lizano, Jorge Canto, Guido Garay, and David Hollenbach. Photoevaporated Flows from H II Regions. *ApJ*, 468:739, September 1996. doi: 10.1086/177729.
- Xing Lu, Qizhou Zhang, Haiyu Baobab Liu, Junzhi Wang, and Qiusheng Gu. Very Large Array Observations of Ammonia in High-mass Star Formation Regions. *ApJ*, 790(2):84, August 2014. doi: 10.1088/0004-637X/790/2/84.
- Jorge Lugo, Susana Lizano, and Guido Garay. Photoevaporated Disks around Massive Young Stars. *ApJ*, 614(2):807–817, October 2004. doi: 10.1086/423924.
- L. T. Maud, T. J. T. Moore, S. L. Lumsden, J. C. Mottram, J. S. Urquhart, and M. G. Hoare. A distance-limited sample of massive molecular outflows. *MNRAS*, 453(1):645–665, October 2015. doi: 10.1093/mnras/stv1635.
- S. Molinari, J. Brand, R. Cesaroni, and F. Palla. A search for precursors of ultracompact HII regions in a sample of luminous IRAS sources. I. Association with ammonia cores. *A&A*, 308: 573–587, April 1996.
- Takumi Nagayama, Hideyuki Kobayashi, Toshihiro Omodaka, Yasuhiro Murata, Ross A. Burns, Mareki Honma, Tomoharu Kurayama, Akiharu Nakagawa, Tomoaki Oyama, Yoshiaki Tamura, and Katsuhisa Sato. Astrometry of Galactic star-forming regions G48.99-0.30 and G49.19-0.34 with VERA: Astrometric accuracy verification of VERA. *PASJ*, 67(4):65, August 2015. doi: 10.1093/pasj/psu129.

- F. M. Olnon. Thermal bremsstrahlung radiospectra for inhomogeneous objects, with an application to MWC 349. *A&A*, 39:217–223, March 1975.
- N. Panagia and M. Felli. The spectrum of the free-free radiation from extended envelopes. *A&A*, 39:1–5, February 1975.
- Nino Panagia. Some Physical parameters of early-type stars. *AJ*, 78:929–934, November 1973. doi: 10.1086/111498.
- J. D. Pandian, K. M. Menten, and P. F. Goldsmith. The Arecibo Methanol Maser Galactic Plane Survey. III. Distances and Luminosities. *ApJ*, 706(2):1609–1624, December 2009. doi: 10.1088/0004-637X/706/2/1609.
- J. D. Pandian, E. Momjian, Y. Xu, K. M. Menten, and P. F. Goldsmith. Spectral energy distributions of 6.7 GHz methanol masers. *A&A*, 522:A8, November 2010. doi: 10.1051/0004-6361/201014937.
- J. D. Pandian, E. Momjian, Y. Xu, K. M. Menten, and P. F. Goldsmith. The Arecibo Methanol Maser Galactic Plane Survey. IV. Accurate Astrometry and Source Morphologies. *ApJ*, 730(1):55, March 2011. doi: 10.1088/0004-637X/730/1/55.
- A. L. Patel, J. S. Urquhart, A. Y. Yang, T. J. T. Moore, K. M. Menten, M. A. Thompson, M. G. Hoare, T. Irbator, S. L. Breen, and M. D. Smith. SCOTCH - search for clandestine optically thick compact H IIs. *MNRAS*, 524(3):4384–4402, September 2023. doi: 10.1093/mnras/stad2143.
- A. L. Patel, J. S. Urquhart, A. Y. Yang, T. Moore, M. A. Thompson, K. M. Menten, and T. Csengeri. SCOTCH - search for clandestine optically thick compact H II regions: II. *MNRAS*, 533(2):2005–2025, September 2024. doi: 10.1093/mnras/stae1910.
- A L Patel, J S Urquhart, A Y Yang, L K Morgan, K M Menten, M A Thompson, T Moore, I Grozdanova, S Khan, and T Csengeri. SCOTCH - III. Complete search for hypercompact H II regions in the fourth quadrant. *MNRAS*, 538(4):2267–2282, April 2025. doi: 10.1093/mnras/staf450.
- N. Peretto and G. A. Fuller. The initial conditions of stellar protocluster formation. I. A catalogue of Spitzer dark clouds. *A&A*, 505(1):405–415, October 2009. doi: 10.1051/0004-6361/200912127.
- J. M. Rathborne, J. M. Jackson, and R. Simon. Infrared Dark Clouds: Precursors to Star Clusters. *ApJ*, 641(1):389–405, April 2006. doi: 10.1086/500423.
- J. M. Rathborne, J. M. Jackson, E. T. Chambers, I. Stojimirovic, R. Simon, R. Shipman, and W. Frieswijk. The Early Stages of Star Formation in Infrared Dark Clouds: Characterizing the Core Dust Properties. *ApJ*, 715(1):310–322, May 2010. doi: 10.1088/0004-637X/715/1/310.
- S. P. Reynolds. Continuum Spectra of Collimated, Ionized Stellar Winds. *ApJ*, 304:713, May 1986. doi: 10.1086/164209.
- L. F. Rodríguez and J. Canto. Stellar winds and molecular clouds : a search for ionized stellar winds. *RMxAA*, 8:163–173, December 1983.
- Luis F. Rodríguez, Ricardo F. González, Gabriela Montes, Hassan M. Asiri, Alejandro C. Raga, and Jorge Cantó. Compact Radio Sources in M17. *ApJ*, 755(2):152, August 2012. doi: 10.1088/0004-637X/755/2/152.

- Tatiana M. Rodríguez, Peter Hofner, Isaac Edelman, Esteban D. Araya, and Viviana Rosero. Searching for Molecular Jets from High-mass Protostars. *ApJS*, 264(2):30, February 2023. doi: 10.3847/1538-4365/aca4c6.
- V. Rosero, P. Hofner, M. Claussen, S. Kurtz, R. Cesaroni, E. D. Araya, C. Carrasco-González, L. F. Rodríguez, K. M. Menten, F. Wyrowski, L. Loinard, and S. P. Ellingsen. Weak and Compact Radio Emission in Early High-mass Star-forming Regions. I. VLA Observations. *ApJS*, 227(2): 25, December 2016. doi: 10.3847/1538-4365/227/2/25.
- Erik Rosolowsky, Miranda K. Dunham, Adam Ginsburg, E. Todd Bradley, James Aguirre, John Bally, Cara Battersby, Claudia Cyganowski, Darren Dowell, Meredith Drosback, Neal J. Evans, II, Jason Glenn, Paul Harvey, Guy S. Stringfellow, Josh Walawender, and Jonathan P. Williams. The Bolocam Galactic Plane Survey. II. Catalog of the Image Data. *ApJS*, 188(1):123–138, May 2010. doi: 10.1088/0067-0049/188/1/123.
- Álvaro Sánchez-Monge, Jagadheep D. Pandian, and Stan Kurtz. Searching for New Hypercompact H II Regions. *ApJL*, 739(1):L9, September 2011. doi: 10.1088/2041-8205/739/1/L9.
- W. M. Schlingman, Y. L. Shirley, D. E. Schenk, E. Rosolowsky, J. Bally, C. Battersby, M. K. Dunham, T. P. Ellsworth-Bowers, N. J. Evans, II, A. Ginsburg, and G. Stringfellow. VizieR Online Data Catalog: The Bolocam Galactic Plane Survey (BGPS). V. (Schlingman+, 2011). VizieR On-line Data Catalog: J/ApJS/195/14. Originally published in: 2011ApJS..195...14S, September 2011.
- T. K. Sridharan, H. Beuther, P. Schilke, K. M. Menten, and F. Wyrowski. High-Mass Protostellar Candidates. I. The Sample and Initial Results. *ApJ*, 566(2):931–944, February 2002. doi: 10.1086/338332.
- Yan Sun, Ye Xu, Xi Chen, Bo Zhang, Yuan-Wei Wu, Christian Henkel, Andreas Brunthaler, Yoon Kyung Choi, and Xing-Wu Zheng. 6.7 GHz methanol maser survey toward GLIMPSE point sources and BGPS 1.1 mm dust clumps. *A&A*, 563:A130, March 2014. doi: 10.1051/0004-6361/201323047.
- M. Szymczak, P. Wolak, A. Bartkiewicz, and K. M. Borkowski. VizieR Online Data Catalog: Torun methanol source catalogue (Szymczak+, 2012). VizieR On-line Data Catalog: J/AN/333/634. Originally published in: 2012AN....333..634S, August 2012.
- Jonathan C. Tan and Christopher F. McKee. Outflow-Confined HII Regions and the Formation of Massive Stars by Accretion. *arXiv e-prints*, art. astro-ph/0309139, September 2003. doi: 10.48550/arXiv.astro-ph/0309139.
- A. Traficante, G. A. Fuller, N. Peretto, J. E. Pineda, and S. Molinari. The initial conditions of stellar protocluster formation - II. A catalogue of starless and protostellar clumps embedded in IRDCs in the Galactic longitude range $15^\circ \leq l \leq 55^\circ$. *MNRAS*, 451(3):3089–3106, August 2015. doi: 10.1093/mnras/stv1158.
- J. S. Urquhart, M. G. Hoare, S. L. Lumsden, R. D. Oudmaijer, T. J. T. Moore, P. R. Brook, J. C. Mottram, B. Davies, and J. J. Stead. The RMS survey. H₂O masers towards a sample of southern hemisphere massive YSO candidates and ultra compact HII regions. *A&A*, 507(2): 795–802, November 2009. doi: 10.1051/0004-6361/200912608.

- J. S. Urquhart, L. K. Morgan, C. C. Figura, T. J. T. Moore, S. L. Lumsden, M. G. Hoare, R. D. Oudmaijer, J. C. Mottram, B. Davies, and M. K. Dunham. The Red MSX Source survey: ammonia and water maser analysis of massive star-forming regions. *MNRAS*, 418(3):1689–1706, December 2011. doi: 10.1111/j.1365-2966.2011.19594.x.
- J. S. Urquhart, T. J. T. Moore, T. Csengeri, F. Wyrowski, F. Schuller, M. G. Hoare, S. L. Lumsden, J. C. Mottram, M. A. Thompson, K. M. Menten, C. M. Walmsley, L. Bronfman, S. Pfalzner, C. König, and M. Wienen. ATLASGAL - towards a complete sample of massive star forming clumps. *MNRAS*, 443(2):1555–1586, September 2014. doi: 10.1093/mnras/stu1207.
- S. Vig, L. Testi, M. Walmsley, S. Molinari, S. Carey, and A. Noriega-Crespo. IRAS 18511+0146: a proto Herbig Ae/Be cluster? *A&A*, 470(3):977–989, August 2007. doi: 10.1051/0004-6361:20077583.
- S. Watt and L. G. Mundy. Molecular Environments of Young Massive Stars: G34.26+0.15, G11.94-0.62, G33.92+0.11, and IRAS 18511+0146. *ApJS*, 125(1):143–160, November 1999. doi: 10.1086/313273.
- S. J. Williams, G. A. Fuller, and T. K. Sridharan. The circumstellar environments of high-mass protostellar objects. I. Submillimetre continuum emission. *A&A*, 417:115–133, April 2004. doi: 10.1051/0004-6361:20031733.
- A. Y. Yang, J. S. Urquhart, M. A. Thompson, K. M. Menten, F. Wyrowski, A. Brunthaler, W. W. Tian, M. Rugel, X. L. Yang, S. Yao, and M. Mutale. A population of hypercompact H II regions identified from young H II regions. *A&A*, 645:A110, January 2021. doi: 10.1051/0004-6361/202038608.
- Luis A. Zapata, Karl Menten, Mark Reid, and Henrik Beuther. An Extensive, Sensitive Search for SiO Masers in High- and Intermediate-Mass Star-Forming Regions. *ApJ*, 691(1):332–341, January 2009. doi: 10.1088/0004-637X/691/1/332.
- Qizhou Zhang, T. R. Hunter, J. Brand, T. K. Sridharan, S. Molinari, M. A. Kramer, and R. Cesaroni. Search for CO Outflows toward a Sample of 69 High-Mass Protostellar Candidates: Frequency of Occurrence. *ApJL*, 552(2):L167–L170, May 2001. doi: 10.1086/320345.
- Qizhou Zhang, T. R. Hunter, J. Brand, T. K. Sridharan, R. Cesaroni, S. Molinari, J. Wang, and M. Kramer. Search for CO Outflows toward a Sample of 69 High-Mass Protostellar Candidates. II. Outflow Properties. *ApJ*, 625(2):864–882, June 2005. doi: 10.1086/429660.